Quantitative estimates of average geomagnetic axial dipole dominance in deep geological time

Andrew J. Biggin[1], Richard K. Bono[1], Domenico G. Meduri[1], Courtney J. Sprain[1,2], Christopher J. Davies[3], Richard Holme[1], Pavel V. Doubrovine[4]

1. Department of Earth, Ocean and Ecological Sciences, University of Liverpool, Liverpool L69 7ZE, UK.
2. Department of Geological Sciences, University of Florida, PO Box 112120, Gainesville, FL 32611-2120, USA.
3. School of Earth and Environment, University of Leeds, Leeds LS2 9JT, UK.
4. Centre for Earth Evolution and Dynamics, University of Oslo, Sem Saelands vei 2A, 0315 Oslo, Norway.

A defining characteristic of the recent geomagnetic field is its dominant axial dipole which provides its navigational utility and dictates the shape of the magnetosphere. Going back through time, much less is known about the degree of axial dipole dominance. Here we use a substantial and diverse set of 3D numerical dynamo simulations and recent observation-based field models to derive a power law relationship between the angular dispersion of virtual geomagnetic poles at the equator and the median axial dipole dominance measured at Earth's surface. Applying this relation to published estimates of equatorial angular dispersion implies that geomagnetic axial dipole dominance averaged over 10^7-10^9 years has remained moderately high and stable through large parts of geological time. This provides an observational constraint to future studies of the geodynamo and palaeomagnetosphere. It also provides some reassurance as to the reliability of palaeogeographical reconstructions provided by palaeomagnetism.

A primary feature of the geomagnetic field today is its strong axial dipole component which provides an effective shield against the solar wind[1, 2] helping to make the planet habitable[3]. The field is highly variable in time however and our knowledge of its morphology declines rapidly as we go back in geological history. At a given instance, the degree of axial dipole (*AD*) dominance over the remaining non axial dipole (*NAD*) components at Earth's surface may be expressed, here, in terms of the Lowes power[4] for the magnetic field energy (*W*) as[5]

$$AD/NAD = W_1^0 / (W - W_1^0) \quad (1)$$

where

$$W = \sum_{n=1}^{n_{max}} \sum_{m=0}^{n} W_n^m \quad (2)$$

and

$$W_n^m = (n+1)[(g_n^m)^2 + (h_n^m)^2] \quad (3)$$

Here g_n^m and h_n^m are the Gauss coefficients of degree *n* and order *m* for the spherical harmonic expansion of the geomagnetic potential[6]; g_1^0 is the axial dipole component.

The current geomagnetic field has *AD/NAD* of approximately 10 (Figure 1) but, according to time-dependent global magnetic field models[7, 8, 9, 10, 11], this has varied by more than one order of magnitude on timescales of kyr (Supplementary Figure 1) over the last 100kyr. By definition, *AD/NAD* must briefly fall to zero during a polarity reversal and can also fall far below unity during excursions[7]. To avoid biasing by brief extreme events, we will take the median of the instantaneous *AD/NAD* ratios which we call AD/NAD_{median} as our measure of average axial dipole dominance. We note that this value is a first-order description of the average, time-instantaneous field morphology and is not intended as a direct measure of the validity of the geocentric axial dipole (GAD[12]) hypothesis which rather would rely on the morphology of the time-average field (TAF). The TAF field is defined by time-averaging all Gauss coefficients independently before using their ratios to define its properties, which may be very different to the properties of the instantaneous field at any and all times. For example AD/NAD_{TAF} is, by definition, infinite for a GAD field whereas the associated AD/NAD_{median} value may be finite and even small. In this sense, AD/NAD_{median} is more relevant to those using palaeomagnetic records to understand geomagnetic behaviour, core dynamics and the magnetospheric shielding it confers than to those interested in making tectonic reconstructions. The implications of this study for palaeogeographical reconstructions is nevertheless explored later.

Direct estimates of AD/NAD_{median} and other useful ratios are possible from statistical field models based on the Giant Gaussian Process[13, 14, 15, 16, 17] spanning back to 10 Ma (Supplementary Table 1). Previous efforts to assess the average morphology of the palaeomagnetic field prior to 10 Ma have been forced to rely on the Model G approach[18] to analysing palaeomagnetic secular variation data. This relies on measurements of the angular dispersion (*S*; *Methods*) of virtual geomagnetic poles (VGPs) recovered from collections of palaeomagnetic recorders (normally lavas). Model G has the form of a second order polynomial:

$$S^2 = a^2 + (b\,\lambda)^2 \qquad (4)$$

where *a* and *b* are constants that define the value of *S* at the equator and the rate of its increase with palaeolatitude (λ) respectively. Using PSV10, a recent compilation of palaeomagnetic secular variation data from rocks formed within the last 10 Myr[19], these Model G constants, given together with their 95% confidence limits, were recently calculated[20] as $a = 11.3^{+1.3}_{-1.1}$ ° and $b = 0.27^{+0.04}_{-0.08}$. For older datasets, the palaeolatitude must be estimated using the palaeomagnetic data themselves and this approach was simulated here (*Methods*).

Using insights from mean-field kinematic dynamo theory and the modern field, McFadden *et al.*[18] made the case that Model G could be used to represent the relative importance of two independent dynamo “families”. The constant *a* denoted the magnitude of the secular variation in the “quadrupole family” comprising those spherical harmonic terms which are symmetric with respect to the equator (and include the equatorial dipole terms). Likewise, *b* did the same for anti-symmetric terms (including the axial dipole) comprising the “dipole family”. In the context of this approach, intervals of time whereby the axial dipole and related antisymmetric terms were particularly dominant over the symmetric terms should be recognisable through increased values of *b* relative to *a* in Model G fits to PSV datasets. Such intervals have previously been argued to include the Cretaceous Normal Superchron[21, 22, 23] and much of Precambrian time[5, 24, 25, 26, 27] but these claims are difficult to verify since the premise on which Model G fits are interpreted is oversimplified[28]. Here we develop and apply a more robust approach to ascertaining information regarding the morphology of the ancient geomagnetic field using palaeosecular variation data.

Model G relationships from dynamo simulations

For the purposes of this study, we use the outputs of 61 numerical dynamo simulations (*Methods*; Supplementary Table 2) which were required to be run for a sufficient amount of time (> 100kyr) to obtain a reasonable temporal sampling of the simulated magnetic field behaviour at the Earth's surface. Each model was distinct in terms of its input parameters and diverse physical ingredients were represented. These included homogeneous and heterogeneous outer boundary heat flux conditions and small and present-day inner core sizes. Models with internal heating sources derived from radiogenic heating, with a stably stratified layer at the top of the core, as well as models where convection is purely chemically driven were also employed (*Methods*). The resulting field behaviour ranges from exhibiting *S* and AD/NAD_{median} values much greater than the Earth's values for recent times to much lower values (Figure 1). In most cases, Model G (after applying a variable cutoff[29] for outliers in VGP distributions) provided a good, though not perfect, fit to VGP dispersion data across the apparent latitudes (Supplementary Table 2) yielding root mean square error *(RMSE)* values with a median across all models of 1.2°. Model G *a* and *b* parameters, together with the powers of the Gauss coefficients (except g_1^0) with degree and order that sum to odd values (W_{ODD}) and even values (W_{EVEN}), are positively correlated (Supplementary Figure 2). As VGP dispersion increases, so does its latitudinal dependence and this reflects increases in the nonaxial-dipole field being partitioned similarly into antisymmetric (given by W_{ODD}) and symmetric (given by W_{EVEN}) terms. We also note in passing that less dipolar simulations in particular tended to produce more complicated curves with an equatorial peak in VGP dispersion (see e.g. LEDA001 in Figure 1). This implies that a reasonable latitudinal distribution of observations is required to obtain both Model G parameters to a good degree of accuracy.

Having ascertained that the structure of Model G (Equation 4) provides efficient two parameter descriptions for a wide range of simulated PSV behaviour, we explored the potential of these simple quadratic fits to predict average morphological characteristics of the generated fields defined as both the median instantaneous and the TAF (Supplementary Figure 3). The most striking observation is a strong power law relation between Model G *a* parameter (average VGP dispersion at the equator; equation 4) and AD/NAD_{median} (Figure 2) that in log-log space reads

$$\log (AD/NAD_{median}) = k_1 \log a + k_2 \tag{5}$$

where the constants and their 95% confidence limits were obtained from standard linear regression: k_1 = -2.26 ± 0.13 ; k_2 = 3.44 ± 0.16. We also observe the following: (1) since Model G *a* and *b* parameters co-vary (Supplementary Figure 2a), the latter is also correlated with AD/NAD_{median} but here the relationship is not quite so strong (Supplementary Figure 3c); (2) the relatively weak relationship between *b/a* and *O/E* implies that the original morphological interpretation of Model G parameters in terms of independent families of equatorially symmetric and antisymmetric spherical harmonic terms[5, 18, 22] is only moderately supported by our dynamo simulations (Supplementary Figure 3a,d); (3) intuitively, Model G parameters provide much stronger constraints on the average instantaneous field morphology (Supplementary Figure 3a,b,c) than the morphology of the time-averaged field (Supplementary Figure 3d,e,f).

The power law (5) presents a potentially powerful new tool linking geomagnetic secular variation and morphology. While the broad observation that enhancing axial dipole dominance suppresses VGP dispersion may be considered intuitive[28], the correlation and significance of the power law (*Adj.* R^2 = 0.955, $P < 10^{-5}$, number of data, N = 61, Spearman rank coefficient ρ = 0.971) is remarkably and unexpectedly high. We note that a power law relationship with similar parameters may also be predicted from simple theoretical arguments (see Supplementary Text).

Testing the correlation using observation-based field models

To ascertain whether time-varying and statistical field models of PSV derived from palaeo- and geo-magnetic observations yield estimates of AD/NAD_median and Model G *a* values which are consistent with the power law in Figure 2, we apply the same analytical approach (Methods) to a selection of these (Supplementary Table 1)[7, 8, 10, 11, 13, 14, 15]. Although similarly represented by sets of Gauss coefficients, the methods of generating these field descriptions are fundamentally distinct to those used to obtain the outputs of the dynamo simulations. While dynamo simulations model field behaviour by numerically solving equations governing the outer core magnetohydrodynamic processes responsible for it, observational models are defined by fitting spatially and temporally restricted datasets of palaeomagnetic, archaeomagnetic and geomagnetic measurements and their associated age estimates. Another important difference is that three of these observational models are restricted to intervals of 9-20kyr which may be too short to capture time-average field behaviour[30]. The statistical models, on the other hand, assume that the statistical properties of paleosecular variation can be modelled by a "Giant Gaussian Process" whereby the Gauss coefficients are randomly drawn from normal distributions with means and variances set to produce the desired characteristics of palaeosecular variation and the time-averaged field [13, 14, 15, 16, 17] (all models assume independently distributed Gauss coefficients except those of ref-16 which assumes a covariance among a select set of Gauss coefficients).

Given the above and the varied AD/NAD_{median} values produced by these observational models (red circles in Figure 2) it is remarkable to observe the Model G parameters are all found close to the power law derived from the dynamo simulations. Indeed, they all fall within an interval (dashed lines) where 95% of future models are predicted to fall according to a t-distribution (*Methods*). We note that we are not overly concerned here with the relative realism of any of the outputs shown by these models, merely the ability of their output palaeosecular variation to predict their average morphology.

The robust nature of this geometric relationship is also supported by the results of an analysis summarised in Figure 3a and Supplementary Figure 3. Here, the g_1^0 term produced at each timestep (or realisation) from three dynamo simulations and one Giant Gaussian Process was rescaled to produce values of AD/NAD_{median} that were radically different from that which the model originally produced (See Supplementary Text for more details). Doing so simultaneously affected the angular dispersion of VGP such that the resulting *a* parameter of the Model G fit fell within the prediction bounds of the earlier derived power law (Figure 3a). This demonstrates that, so long as the power spectrum of the nondipole field is consistent with any of these models, the relationship is robust to a large range of AD/NAD_{median} values.

Based on the evidence presented in figures 2 and 3a, Equation 5 and its associated prediction bounds appear consistent with all available empirical and synthetic datasets. We therefore consider it to provide a robust description of the relationship between geomagnetic variability and morphology allowing reliable estimates of one to act as a proxy for the other.

Estimating geomagnetic axial dipole dominance in ancient times

Figure 3b,c and Supplementary Figure 4 demonstrate two further useful properties of the power law relation outlined above. Firstly, although AD/NAD_{median} may change significantly for subintervals within a single model time series, the associated Model G *a* parameter from the same subinterval also shifts according to the power law. This implies that selections of palaeomagnetic datasets from any interval duration may be useful for estimating the average axial dipole dominance for that same interval. A caveat is that the interval must be sufficiently long such that significant serial correlation of VGP positions is avoided. Based on our sliding window analysis of both observational models and dynamo simulations (Figure 3b, Supplementary Figure 4), 50-100kyr appears to be sufficient for this purpose; this duration is similar to earlier estimates of the time necessary to sample the time-averaged field[30].

The second useful property of the power law relation is that it remains capable of accurately estimating AD/NAD_{median} even when the number of locations and time steps used to construct the Model G curve are reduced to values that are well within the bounds of palaeomagnetic datasets available for ancient intervals. Table 1 presents a selection of recent published estimates of Model G *a* parameters for intervals extending back into the Archaean[19, 20, 27]. The smallest number of locations comprising any single one of these datasets is 19 while the smallest median number of sampling sites per location (representative of time steps) is 15. These values were used as conservative inputs for the downsampling of models (*Methods*) whose results are summarised in Figure 3c (see also Supplementary Figure 4). So long as the interval is sufficiently long (> 50 kyr), the estimates of AD/NAD_{median} were found to be nearly always reliable (accurate, if not necessarily precise).

Figure 4a presents estimates of AD/NAD_{median} calculated using the Model G *a* parameter for the five studied intervals listed in Table 1. In each case, the Model G parameters were taken directly from the publications and required application of the Vandamme cutoff[29] as used for all models here. These intervals are far longer than the time spanned by any one of the individual estimates of VGP angular dispersion from which the Model G fits were constructed. Furthermore, in the earlier intervals in particular, there are large gaps in the age distribution of the rocks used to obtain the estimate. Therefore, values of AD/NAD_{median} cited for each period should be considered as weighted towards sub-intervals with denser data coverage (Figure 4a) and may not be representative of sub-intervals (of which 600-1100 Ma is the most striking) where no or very little data currently exists. A further point to note is that AD/NAD_{median} values will also be more heavily influenced by those rock units with low apparent palaeolatitudes since they exert more influence on the *a* parameter of the Model G fit.

The above caveats notwithstanding, the degree of stationarity displayed by our obtained estimates of AD/NAD_{median} is remarkable (Figure 4a). Uncertainty limits on AD/NAD_{median}, calculated by combining uncertainties associated with the Model G *a* parameters with the power law prediction bounds, render each time interval indistinguishable from the rest. Furthermore, the total range observed in estimated AD/NAD_{median} values (including uncertainty limits) from 3.5 to 45.0 encompasses the values derived from observation-based field models covering intervals in more recent geological time (Figure 2).

While axial dipole dominance apparently changes rapidly on short timescales (Supplementary Figure 1) and is prone to collapse during geomagnetic excursions and reversal transitions, we presently find no evidence that its average over 10^7 to 10^9 year timescales is subject to significant variations. Given that *AD/NAD* must instantaneously reach zero for a reversal to take place, a particularly surprising insight is that intervals with substantially different reversal frequencies (e.g. the last 10 Myr, the Cretaceous Normal Superchron, and the early Cretaceous-Jurassic) apparently yield nearly identical values of AD/NAD_{median} (Figure 4a). This implies that, regardless of how frequently *AD/NAD* undergoes brief collapse, the field recovers to spend most of its time in a similarly dipole dominated state. Intervals of stable average axial dipole dominance also apparently coincided with significant variations in long term average field intensity[31, 32, 33]. This further suggests that the magnitude of the axial dipole and non-axial dipole field are correlated on long-timescales such that the degree of axial dipole dominance remains approximately constant. These coupled observations may be used as constraints for future geodynamo modelling studies seeking to capture long term variations in geomagnetic field behaviour.

Changes in aspects of geodynamo behaviour are thought likely to result from secular changes in core cooling modulated by mantle convection over the last several billion years[33, 34, 35, 36, 37, 38, 39]. Indeed the changing nature of the forcing of outer core convection from both above and below implies that it is already a challenge to explain how the geomagnetic field has been continuously sustained over Earth history[40]. Here we add the further constraint that models should produce a similar average geomagnetic field morphology for much of a time period where the Earth has seen its liquid core nucleate and grow an inner core[41] and the mantle undergo several supercontinent cycles[42] with consequences expected for core-mantle heat flow and its pattern[43].

Almost all of the numerical dynamo simulations performed in a study[44] aiming to elucidate the magnetic signature of inner core nucleation gave values of axial dipole dominance within the range implied by the palaeomagnetic datasets used here (J. Aubert, pers. Comm.). This suggests that diverse core geometries, control parameters, forcing conditions etc are capable of giving rise to field morphologies similar to those associated with Earth in the past. Nevertheless, it is important to highlight that our analysis of palaeomagnetic datasets does not rule out exotic field morphologies (e.g. extreme multipolar or equatorial dipole dominated[45]) existing for some times in the past. These could be missed either because of insufficient palaeomagnetic data coverage (figure 4) or because their behaviour (and especially their power spectra) is outside the range of models used to constrain the power law tested here.

Our findings also have implications for Earth's palaeo-magnetosphere and the long-term shielding of Earth's atmosphere from solar wind. The strong and dominantly axial dipolar morphology of the present-day geomagnetic field is an efficient one for reducing fluxes of energetic particle into Earth's upper and middle atmosphere and restricting these to high latitudes[46]. Large reductions in axial dipole dominance, even while maintaining the same dipole moment (e.g. in a pure dipole rotation scenario) are expected to cause polar caps, auroral zones and atmospheric impacts of solar energetic particles to migrate to lower latitudes[1, 47]. For the time periods considered, our results suggest that such major decreases in axial dipole dominance are relatively rare, being restricted to the extremes of reversals and excursions.

A primary application of palaeomagnetism is to produce palaeogeographic reconstructions, making use of the geocentric axial dipole (GAD) model to relate changes in mean inclination to inferred shifts in palaeolatitude. Values of AD/NAD_{median} cannot be interpreted directly as measures of the validity of the GAD approximation of the time-averaged field because they are constructed using different averaging processes (specifically, the former is the average of multiple instantaneous global field morphologies whereas the latter is the field produced by the average of multiple directional measurements, i.e. the time-averaged power spectrum, and yields AD/NAD_{TAF} values in these models of approximately one order of magnitude higher). Nevertheless, our dynamo simulations do show correlations between their Model G parameters and AD/NAD_{TAF} (Supplementary Figure 3) and, most usefully, exhibit a statistically significant relationship between the Model G a parameter, used here to estimate the AD/NAD_{median} values, and the maximum absolute inclination anomaly, a direct and commonly used (e.g. ref. 18) measurement of the validity of GAD (Figure 4b; *Methods*). Furthermore, our actual measurements of these two parameters using rocks from the last 10 million years[19] also fit this trend very well. We point out that while the peak inclination anomalies in both the dynamo models and the PSV10 dataset tend to produce shallower than expected directions, the peak in the models is nearly always observed at latitudes of 25-30° (north or south; appendix 1) whereas in the data it is within 10° of the equator[19]. If we nevertheless take the relationship in Figure 4b at face value, the range of published Model G a parameters from much older datasets suggest that its violations for the time periods studied here are unlikely to be much more severe than that measured for the last 10 Myr. A recent study[48] claimed that the model underlying the inclination anomalies measured for the past 10 Myr may be GAD; if this is true, then we cannot discount GAD for any of the periods examined here.

The overall picture emerging from this study is of a geomagnetic field whose average morphology has been extraordinarily uniformitarian in the face of substantial changes in geodynamo forcing that impacted on its strength and tendency to reverse polarity. It should be emphasised that this does not preclude the past occurrence of intervals of sustained highly anomalous field behaviour that also presented distinctive morphological characteristics (e.g. the mid-Palaeozoic[49, 50] and Ediacaran[33, 51] are both potential candidates for such times). It would, however, seem to require that such intervals are relatively rare and do not include the most recent superchron.

Methods

Calculation of virtual geomagnetic pole dispersion and Model G fits. Outputs of magnetic field at Earth's surface were extracted from numerical dynamo and observational models in the form of 120 Gauss coefficients (i.e. up to degree and order 10) for each regularly spaced time realisation. We truncate the numerical dynamo simulation results to degree and order 10 in order to make them compatible with the highest resolution available in the observational models considered here.

In all analyses, except for those employing "down sampling" (Figure 3b,c and Supplementary Figure 4), 324 locations spaced 20° apart in longitude (between 0° and 340°) and 10° apart in latitude (between -85° and 85°) were analysed and 500 different sets of random timesteps were chosen at each of these. Note that this geographical sampling was deliberately chosen to be far from uniform (being very heavily concentrated at high latitudes) in order to define Model G equally well at all latitudes.

From each set of Gauss coefficients, we synthesized a magnetic field vector at the specified location and used its direction (expressed by declination and inclination) to represent an independent palaeomagnetic direction. Conversion to virtual geomagnetic poles (VGPs) followed standard palaeomagnetic convention[52]. VGPs were then grouped by location, flipped to give a common polarity (i.e., the VGPs falling into the southern hemisphere were replaced by antipodal locations in the northern hemisphere), and used to produce 324 estimates of apparent palaeolatitude (λ) and VGP dispersion (*S*). λ was calculated using the great-circle distance between the mean VGP position and the site location. *S* was initially defined from the root mean square angular distances (Δ_i) between the i-th VGP and the mean VGP position according to

$$S = \left[\frac{1}{N-1}\sum_{i=1}^{N} {\Delta_i}^2\right]^{1/2} \qquad \text{(M1)}$$

where *N* is the total number of VGPs (500 in this case). This approach has been applied to all palaeomagnetic datasets used in our study, except for the 0-10 Ma dataset, and was therefore simulated here.

An iterative procedure was then used to exclude outliers at each location caused by reversal transitions and excursions following the well-established variable cut-off approach of Vandamme[29].

Model G (Equation 4) was fit to curves comprising the 324 $\lambda - S$ pairs calculated above using a least-squares minimisation algorithm within the optimisation toolbox of *Matlab* using a bounded search, where the limits are conservatively set for Model G *a* and *b* parameters (1 to 90° and 0 to 1, respectively). With the exception of the lower bound for b, all Model G fits fall far from the boundaries used in the minimisation.

The procedure for obtaining Model G parameters from down-sampled models was identical to the above except that *N* at each location was reduced from 500 to 15 and the number of locations was reduced from 324 to 19 which were randomly drawn from a uniform distribution on a sphere.

Numerical dynamo simulations. Most of the numerical geodynamo models employed in this study have been extensively described elsewhere[53, 54, 55, 56] and we thus outline only the essentials here. An electrically conducting and convecting Boussinesq fluid is confined in a spherical shell of thickness $d = r_o - r_i$, where r_i and r_o denote the inner and outer boundary radii respectively. The spherical shell rotates about the vertical direction with angular frequency Ω. As detailed in ref. 51, we solve numerically the momentum equation for the fluid velocity $\boldsymbol{u}$ in the co-rotating frame of reference, the induction equation for the magnetic field $\boldsymbol{B}$, and an equation of evolution for the temperature perturbations T. The equations are non-dimensionalised using the shell thickness d as length scale, the core magnetic diffusion time $\tau_\eta = d^2/\eta$ as time scale, while $(2\Omega\rho\mu_0\eta)^{1/2}$ serves to rescale the magnetic field. Here η denotes the outer core magnetic diffusivity, ρ the core fluid density, and μ_0 the vacuum permeability. Five dimensionless parameters control the system: the shell aspect ratio

$$\chi = \frac{r_i}{r_o}, \qquad \text{(M2)}$$

the Ekman number

$$E = \frac{\nu}{2\Omega d^2}, \qquad \text{(M3)}$$

the Prandtl number

$$Pr = \frac{\nu}{\kappa}, \qquad \text{(M4)}$$

the magnetic Prandtl number

$$Pm = \frac{\nu}{\eta}, \qquad \text{(M5)}$$

and the modified Rayleigh number

$$Ra = \frac{\alpha g_o \delta T\, d}{2\Omega\kappa}. \qquad \text{(M6)}$$

Here ν, κ, and α are the fluid kinematic viscosity, thermal diffusivity, and thermal expansivity respectively; g_o is gravity at the outer boundary and δT is a temperature scale that depends on the temperature boundary conditions and on the internal heating mode (see ref. 48 and ref. 52 for further details).

Supplementary Table 2 lists values of the above input parameters for all the numerical simulations employed in this study. All simulations have $Pr = 1$. With the exception of three models with smaller inner core sizes, we consider a present-day outer core aspect ratio of $\chi = 0.35$. All simulations employ no-slip flow boundary conditions. The inner core and the mantle are considered electrically insulating, thus the magnetic field at r_i and at r_o matches the respective potential field outside of the dynamo region. As for the thermal boundary conditions, fixed heat flux (FF) is imposed at r_o in all simulations. FF or fixed temperature (FT) conditions are used at r_i. Some simulations employ spatial variations in the outer boundary heat flux. In most of these cases, the imposed heat flux heterogeneity pattern is a recumbent spherical harmonic of degree 2 and order 0 (recumbent Y_2^0) that approximates the large scale structure of the observed lower mantle seismic shear-wave anomalies [58]. Three models are instead based on the lower mantle tomographic model of shear-wave velocity of ref. 59. The heterogeneity amplitude is defined by the parameter

$$\epsilon = \frac{q_{max} - q_{min}}{\langle q \rangle} \qquad \text{(M7)}$$

where q_{min} and q_{max} are the minimum and maximum values of the outer boundary heat flux respectively, and $\langle q \rangle$ is its mean value. Values of ϵ range from 0.3 to 1.5 in our numerical simulations (see Supplementary Table 2).

In the suite of simulations considered in this study, 37 have been reported in ref-55 (a subset of these are previously published models; see Supplementary Table 1) and we thus do not describe them in detail here. We additionally employed 24 new simulations here. Among these, 3 include a uniform internal heat source term in the temperature equation modelling the presence of radiogenic heating (or secular cooling of the core). In several of these new models convection is purely chemically driven, that is the source of buoyancy is the release of light elements at the inner core boundary as the inner core freezes. Finally, some models allow for the presence of a stably stratified layer at the top of the core. We now briefly describe the formulation employed to model these different physical characteristics of the core. The equation of evolution for the temperature perturbations T around the background (adiabatic) reference state is

$$\frac{\partial T}{\partial t} + (u \cdot \nabla)T = q\nabla^2 T + q\,\gamma. \qquad \text{(M8)}$$

Here $q = \kappa/\eta$ is the Roberts number, which is related to the input model parameters by $q = Pm/Pr$, and γ is a uniform volumetric sink ($\gamma < 0$) or source ($\gamma > 0$) term. The stationary background temperature profile is given by

$$\frac{dT_0}{dr} = -\frac{\gamma}{3}r - \frac{1}{r^2} \qquad \text{(M9)}$$

with $\gamma = \gamma' d^2/\kappa\delta T$, where γ' denotes the dimensional heat source/sink amplitude. A volumetric sink term and a zero heat flux condition at the outer boundary are appropriate for modelling purely chemical convection [60, 61]. In this case, the variable T here is interpreted as the concentration of light elements in the core that are released at the inner core boundary. From Eq. (M9), a zero flux condition at r_o sets the value of the sink term to $\gamma = -3(1-\chi)^3$. For $\chi = 0.35$, the present-day outer core aspect ratio, then $\gamma \approx -0.824 = \gamma_0$. For values $\gamma < \gamma_0$, the neutrally buoyant radius r_* falls within the fluid interior. Convection thus occurs for $r < r_*$, while the region $r > r_*$ is sub-adiabatic and mimics the presence of a stably stratified layer at the top of the core. In our numerical simulations, we used either $\gamma = -1.14$ or $\gamma = -1.44$ (see Supplementary Table 2), which correspond to a stably stratified layer at the top of the core of thickness of about $\delta/d = 0.16$ and $\delta/d = 0.26$, respectively. In one case we explored the effect of an extreme stably stratified layer thickness of 0.54 (γ = -3).

Time is rescaled to physical units based on the electrical conductivity estimates provided by ref. 62 which suggests τ_η = 200 kyr. All models were truncated such that transient effects associated with initialisation were excluded. The individual Gauss coefficients were then temporally resampled using a cubic spline fit in order to yield regularly spaced time steps.

Regression and calculation of uncertainties. Uncertainties for the estimates of AD/NAD_{median} calculated for the palaeomagnetic datasets (Table 1, Figure 4a) and the downsampled models (figure 3b,c) combined errors in the prediction of the power law (Figure 2) and in the Model G *a* parameter. The former were 95% prediction bounds on the power law displayed in Figure 2 calculated using standard linear regression analysis and a t-distribution (*Matlab* curve-fitting toolbox and *predint* function using default settings) performed on the datasets in log-space. Although these techniques strictly assume Gaussian bivariate distributions, they are demonstrably effective here in encompassing the majority of the data. The latter consisted of 95% confidence bounds calculated using 1000 or 10000 bootstraps resampling with replacement. Combining these two errors into a single uncertainty for estimated AD/NAD_{median} allowed for the full overlap of error bars and the shaded region in Figure 3c producing a conservative range whose usefulness is supported by the down-sampling results displayed in Figure 3b and c and Supplementary Figure 4.

Acknowledgements

AJB, CJS and CJD acknowledge support from the Natural Environment Research Council (standard grant, NE/P00170X/1); AJB, RKB, and DGM acknowledge support from The Leverhulme Trust (Research Leadership Award, RL-2016-080); PVD acknowledges support from the Research Council of Norway through its Centres of Excellence funding scheme, project 646 number 223272 (CEED).

Author Contributions

AJB designed the study and performed the analyses. RKB, DGM, CJS and CJD performed new dynamo simulations and analyses. PVD derived the theoretical power law. All authors contributed to writing the paper.

Data availability Statement

The datasets generated during and/or analysed during the current study are available from the corresponding author on reasonable request.

Code availability

The code used to perform these analyses are available from the corresponding author on reasonable request.

References

1. Zossi B, Fagre M, Amit H, Elias AG. Polar caps during geomagnetic polarity reversals. *Geophys J Int* 2019, **216:** 1334-1343.

2. Siscoe GL, Sibeck DG. Effects of nondipole components on auroral zone configurations during weak dipole field epochs. *J Geophys Res* 1980, **87:** 3549-3556.

3. Tarduno JA, Cottrell RD, Watkeys MK, Hofmann A, Doubrovine PV, Mamajek EE*, et al.* Geodynamo, Solar Wind, and Magnetopause 3.4 to 3.45 Billion Years Ago. *Science* 2010, **327**(5970)**:** 1238-1240.

4. Lowes FJ. Spatial Power Spectrum of the Main Geomagnetic Field, and Extrapolation to the Core. *Geophys J Roy Astr S* 1974, **36:** 717-730.

5. Coe RS, Glatzmaier GA. Symmetry and stability of the geomagnetic field. *Geophys Res Lett* 2006, **33**(21)**:** 2006GL027903.

6. Langel RA. The Main field. In: Jacobs JA (ed). *Geomagnetism*, vol. 1. Academic Press: London, UK, 1987, pp 249-512.

7. Brown MC, Korte M, Holme R, Wardinski I, Gunnarson S. Earth's magnetic field is probably not reversing. *P Natl Acad Sci USA* 2018, **115:** 5111-5116.

8. Constable C, Korte M, Panovska S. Persistent high paleosecular variation activity in southern hemisphere for at least 10000 years. *Earth Planet Sc Lett* 2016, **453:** 78-86.

9. Jackson A, Jonkers ART, Walker MR. Four centuries of geomagnetic secular variation from historical records. *Philosophical Transactions of the Royal Society of London Series a-Mathematical Physical and Engineering Sciences* 2000, **358**(1768)**:** 957-990.

10. Nilsson A, Holme R, Korte M, Suttie N, Hill M. Reconstructing Holocene geomagnetic field variation: new methods, models and implications. *Geophys J Int* 2014, **198:** 229-248.

11. Panovska S, Constable C, Korte M. Extending Global Continuous Geomagnetic Field Reconstructions on Timescales Beyond Human Civilization. *Geochem Geophy Geosy* 2018, **19:** 4757-4772.

12. Creer KM, Irving J, Runcorn SK. The direction of the geomagnetic field in remote epochs in Great Britain. *J Geomagn Geoelectr* 1954, **6:** 163-168.

13. Constable C, Johnson C. Anisotropic paleosecular variation models: implications for geomagnetic field observables. *Phys Earth Planet In* 1999, **115:** 35-51.

14. Constable CG, Parker RL. Statistics of the Geomagnetic Secular Variation for the Past 5-My. *J Geophys Res-Solid* 1988, **93**(B10)**:** 11569-11581.

15. Tauxe L, Kent DV. A simplified statistical model for the geomagnetic field and the detection of shallow bias in paleomagnetic inclinations: was the ancient magnetic field dipolar? *AGU Geophysical Monograph Series* 2004, **145:** 101-115.

16. Bono RK, Biggin AJ, Holme R, Davies C, Meduri DG, Bestard J. Covariant Giant Gaussian Process Models with Improved Reproduction of Palaeosecular Variation. *Geochem Geophy Geosy* 2020, **21:** e2020GC008960.

17. Brandt D, Constable C, Ernesto M. Giant Gaussian process models of geomagnetic palaeosecular variation: a directional outlook. *Geophys J Int* 2020, **222:** 1526-1541.

18. McFadden PL, Merrill RT, McElhinny MW. Dipole Quadrupole Family Modeling of Paleosecular Variation. *J Geophys Res-Solid* 1988, **93**(B10)**:** 11583-11588.

19. Cromwell G, Johnson CL, Tauxe L, Constable C, Jarboe N. PSV10: a global data set for 0-10 Ma time-averaged field and paleosecular variation studies. *Geochem Geophy Geosy* 2018, **DOI 10.1002/2017GC007318**.

20. Doubrovine PV, Veikkolainen T, Pesonen L, Piispa E, Ots S, Smirnov AV*, et al.* Latitude dependence of geomagnetic paleosecular variation and its relation to the frequency of magnetic reversals: Observations from the Cretaceous and Jurassic. *Geochem Geophy Geosy* 2019, **20:** 1240-1279.

21. Biggin AJ, van Hinsbergen D, Langereis CG, G.B. S, Deenen MHL. Geomagnetic Secular variation in the Cretaceous Normal Superchron and in the Jurassic. *Phys Earth Planet In* 2008, **169:** 3-19.

22. McFadden PL, Merrill RT, McElhinny MW, Lee SH. Reversals of the Earths Magnetic-Field and Temporal Variations of the Dynamo Families. *J Geophys Res-Solid* 1991, **96**(B3)**:** 3923-3933.

23. Tarduno JA, Cottrell RD, Smirnov AV. The Cretaceous superchron geodynamo: Observations near the tangent cylinder. *P Natl Acad Sci USA* 2002, **99**(22)**:** 14020-14025.

24. Biggin AJ, Strik GHMA, Langereis CG. Evidence for a very-long-term trend in geomagnetic secular variation. *Nat Geosci* 2008, **1**(6)**:** 395-398.

25. Smirnov AV, Tarduno JA. Secular variation of the Late Archean Early Proterozoic geodynamo. *Geophys Res Lett* 2004, **31**(16)**:** 10.1029/2004GL020333.

26. Smirnov AV, Tarduno JA, Evans DAD. Evolving core conditions ca. 2 billion years ago detected by paleosecular variation. *Phys Earth Planet In* 2011, **187**(3-4)**:** 225-231.

27. Veikkolainen T, Pesonen LJ. Palaeosecular variation, field reversals and the stability of the geodynamo in the Precambrian. *Geophys J Int* 2014, **199**(3)**:** 1515-1526.

28. Hulot G, Gallet Y. On the interpretation of virtual geomagnetic pole (VGP) scatter curves. *Phys Earth Planet In* 1996, **95**(1-2)**:** 37-53.

29. Vandamme D. A New Method to Determine Paleosecular Variation. *Phys Earth Planet In* 1994, **85**(1-2)**:** 131-142.

30. Merrill RT, McFadden PL. The geomagnetic axial dipole field assumption. *Phys Earth Planet In* 2003, **139**(3-4)**:** 171-185.

31. Biggin AJ, Piispa EJ, Pesonen LJ, Holme R, Paterson GA, Veikkolainen T*, et al.* Palaeomagnetic field intensity variations suggest Mesoproterozoic inner-core nucleation. *Nature* 2015, **526**(7572)**:** 245-248.

32. Kulakov EV, Sprain CJ, Doubrovine PV, Smirnov AV, Paterson GA, Hawkins L*, et al.* Analysis of an updated paleointensity database (QPI-PINT) for 65-200 Ma: Implications for the long-term history of dipole moment through the Mesozoic. *J Geophys Res* 2019, **124:** doi: 10.1029/2018JB017287.

33. Bono RK, Tarduno JA, Nimmo F, Cottrell RD. Young inner core inferred from Ediacaran ultra-low geomagnetic field intensity. *Nat Geosci* 2019, **12:** 143–147.

34. Aubert J, Labrosse S, Poitou C. Modelling the palaeo-evolution of the geodynamo. *Geophys J Int* 2009, **179:** 1414-1428.

35. Driscoll P. Simulating 2 Ga of geodynamo history. *Geophys Res Lett* 2016, **43:** 5680-5687.

36. Biggin AJ, Steinberger B, Aubert J, Suttie N, Holme R, Torsvik TH*, et al.* Possible links between long-term geomagnetic variations and whole-mantle convection processes. *Nat Geosci* 2012, **5**(8)**:** 526-533.

37. Buffett BA. Core-mantle interactions. In: Olson P (ed). *Core Dynamics*, vol. 8. Elsevier: Amsterdam, 2015, pp 213-224.

38. Hounslow M, Domeier M, Biggin AJ. Subduction flux modulates the geomagnetic polarity reversal rate. *Tectonophysics* 2018, **742-743:** 34-49.

39. Olson PL, Deguen R, Hinnov LA, Zhong SJ. Controls on geomagnetic reversals and core evolution by mantle convection in the Phanerozoic. *Phys Earth Planet In* 2013, **214:** 87-103.

40. Olson P. The New Core Paradox. *Science* 2013, **342:** 431-432.

41. Davies C, Pozzo M, Gubbins D, Alfe D. Constraints from material properties on the dynamics and evolution of Earth's core. *Nat Geosci* 2015, **8**(9)**:** 678-685.

42. Li ZX, Mitchell RN, Spencer CJ, Ernst R, Pisarevsky S, Kirscher U*, et al.* Decoding Earth's rhythms: Modulation of supercontinent cycles by longer superocean episodes. *Precambrian Res* 2019, **323:** 1-5.

43. Zhang N, Zhong SJ. Heat fluxes at the Earth's surface and core-mantle boundary since Pangea formation and their implications for the geomagnetic superchrons. *Earth Planet Sc Lett* 2011, **306**(3-4)**:** 205-216.

44. Landeau M, Aubert J, Olson P. The signature of inner-core nucleation on the geodynamo. *Earth Planet Sc Lett* 2017, **465:** 193-204.

45. Abrajevitch A, Van der Voo R. Incompatible Ediacaran paleomagnetic directions suggest an equatorial geomagnetic dipole hypothesis. *Earth Planet Sc Lett* 2010, **293**(1-2)**:** 164-170.

46. Vogt J, Zieger B, Glassmeier KH, Stadelmann A, Kallenrode M-B, Sinnhuber M*, et al.* Energetic particles in the paleomagnetosphere: Reduced dipole configurations and quadrupolar contributions. *J Geophys Res* 2007, **112:** A06216.

47. Winkler H, Sinnhuber M, Notholt J, Kallenrode M-B, Steinhilber F, Vogt J*, et al.* Modeling impacts of geomagnetic field variations on middle atmospheric ozone responses to solar proton events on long timescales. *J Geophys Res* 2008, **113:** D02302.

48. Behar N, Shaar R, Tauxe L, Asefaw H, Ebert Y, Heimann A*, et al.* Paleomagnetism and Paleosecular Variations From the Plio-Pleistocene Golan Heights Volcanic Plateau, Israel. *Geochem Geophy Geosy* 2019, **20:** https://doi.org/10.1029/2019GC008479.

49. Hawkins L, Anwar T, Shcherbakova VV, Biggin AJ, Kravchinsky VA, Shatsillo A*, et al.* An exceptionally weak Devonian geomagnetic field recorded by the Viluy Traps, Siberia. *Earth Planet Sc Lett* 2019, **506:** 134-145.

50. Shcherbakova VV, Biggin AJ, Veselovskiy RV, Shatsillo AV, Hawkins LMA, Shcherbakov VP*, et al.* Was the Devonian geomagnetic field dipolar or multipolar? Palaeointensity studies of Devonian igneous rocks from the Minusa Basin (Siberia) and the Kola Peninsula dykes, Russia. *Geophys J Int* 2017, **209:** 1265-1286.

51. Meert JG, Levashova NM, Bazhenov ML, Landing E. Rapid changes in magnetic field polarity during the Late Ediacaran: Trigger for the agronomic revolution and demise of the Ediacaran fauna? . *Gondwana Res* 2016, **34:** 149-157.

52. Butler RF. *Paleomagnetism: Magnetic Domains to Geologic Terranes*. Blackwell Scientific Publications: Oxford, 1992.

53. Davies C, Constable C. Insights from geodynamo simulations into long-term geomagnetic field behaviour. *Earth Planet Sc Lett* 2014, **404:** 238-249.

54. Davies C, Gubbins D. A buoyancy profile for Earth's core. *Geophys J Int* 2011, **187:** 549-563.

55. Sprain CJ, Biggin AJ, Davies CJ, Bono RK, Meduri DG. An assessment of long duration geodynamo simulations using new paleomagnetic modeling criteria (QPM). *Earth Planet Sc Lett* 2019, **526:** 115758.

56. Willis AP, Sreenivasan B, Gubbins D. Thermal core–mantle interaction: Exploring regimes for 'locked' dynamo action. *Phys Earth Planet In* 2007, **165:** 83-92.

57. Davies C, Gubbins D, Willis A, Jimack P. Time-averaged paleomagnetic field and secular variation: Predictions from dynamo solutions based on lower mantle seismic tomography. *Phys Earth Planet In* 2008, **169:** 194-203.

58. Dziewonski AM, Lekic V, Romanowicz BA. Mantle Anchor Structure: An argument for bottom up tectonics. *Earth Planet Sc Lett* 2010, **299**(1-2)**:** 69-79.

59. Masters G, Johnson S, Laske G, Bolton H. A shear-velocity model of the mantle. Philos. Trans. R. Soc. A354, 1385–1411. *Philosophical Transactions of the Royal Society* 1996, **A354:** 1385-1411.

60. Braginsky S, Roberts P. Equations governing convection in Earth's core and the geodynamo. *Geophysical and Astrophysical Fluid Dynamics* 1995, **79:** 1-97.

61. Kutzner C, Christensen UR. Effects of driving mechanisms in geodynamo models. *Geophys Res Lett* 2000, **27:** 29-32.

62. Pozzo M, Davies C, Gubbins D, Alfè D. Thermal and electrical conductivity of iron at Earth's core conditions. *Nature* 2012, **485:** 355-358.

63. Thébault Eea. International Geomagnetic Reference Field: the 12th generation. *Earth, Planets and Space* 2015, **67:** 79.

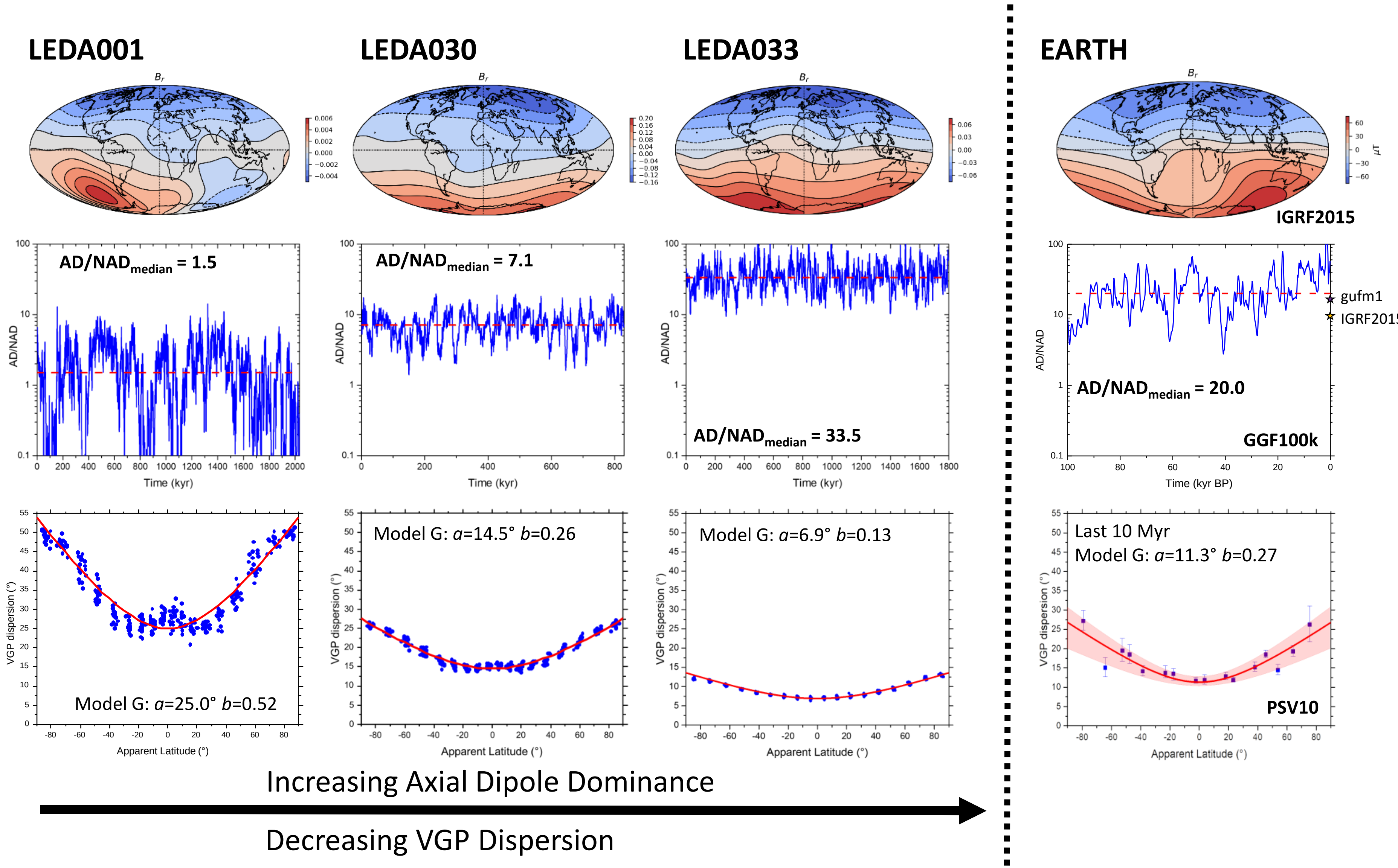

Figure 1: Summary of magnetic field behaviour from representative geodynamo simulations (first three columns) showing tendency of AD/NAD_{median} to increase as VGP dispersion decreases. The first row is a snapshot of radial field at the Earth's surface taken from a timestep with *AD/NAD* close to its median for the time series shown in the second row (median shown as red line; note the semi-log scale). The third row represents palaeosecular variation as presented in studies of ancient time periods (but with far more data); the red line represents the best Model G fit (parameters *a* and *b* provided) to the entire data set of 500 randomly drawn timesteps (blue circles) sampled at each of 324 regularly placed locations (see *Methods*). Final column: equivalent plots for observational geomagnetic models[11,63] and a palaeosecular variation dataset from last 10 Myr[19]. Note that *AD/NAD* for IGRF2015 is 9.6 and AD/NAD_{median} for gufm1 is 16.4. The red shaded area around the Model G fit to the empirical data represents 95% confidence bounds.

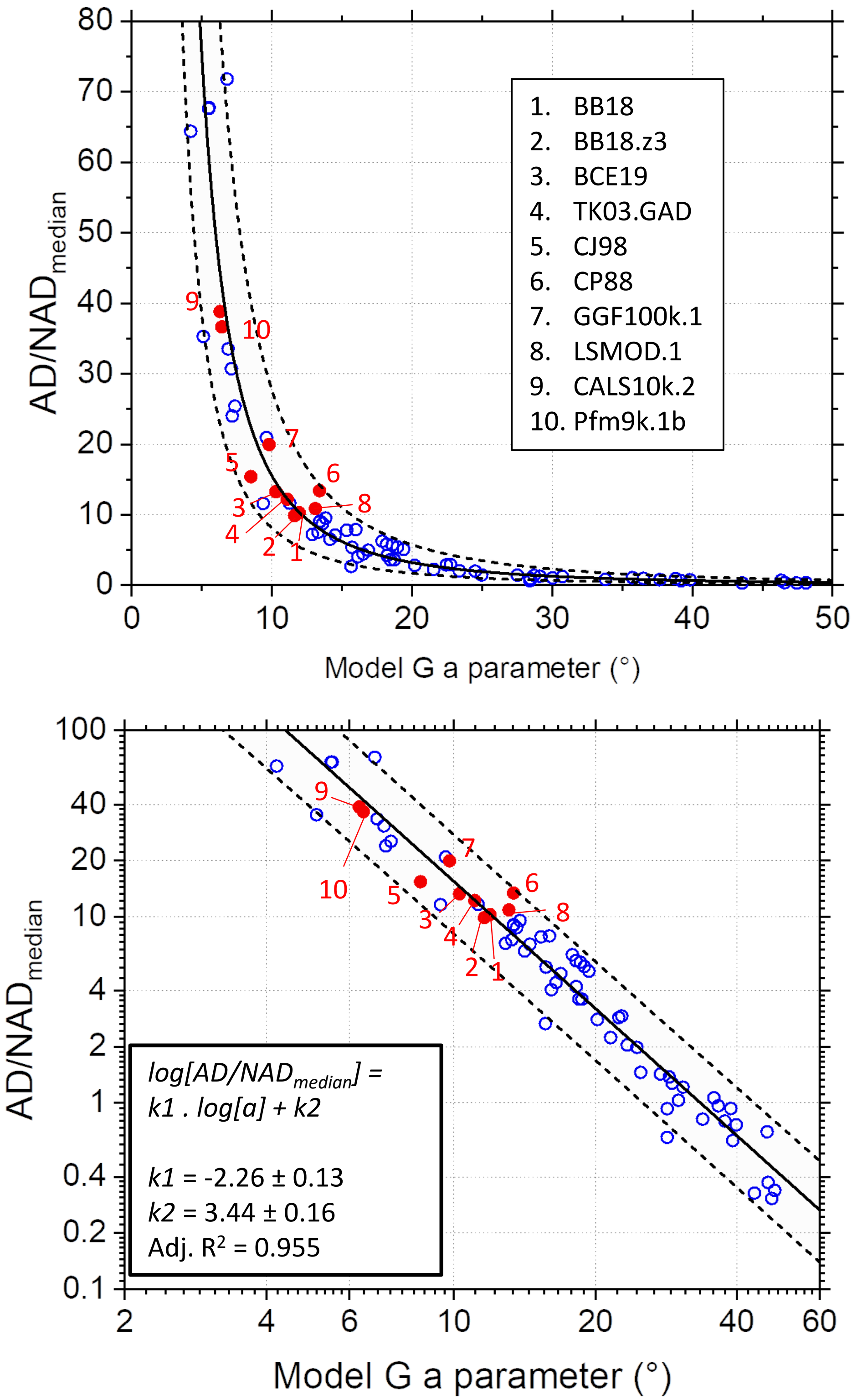

Figure 2: Power law relationship, shown on linear (top) and log axes (bottom), enabling estimation of first order geomagnetic field morphology from palaeosecular variation analysis. Red points are observation-based models (Supplementary Table 1) testing the relationship which is based entirely on dynamo simulation outputs (blue hollow points; Supplementary Table 2). Shaded area is 95% prediction bounds calculated from a linear regression performed in log-space.

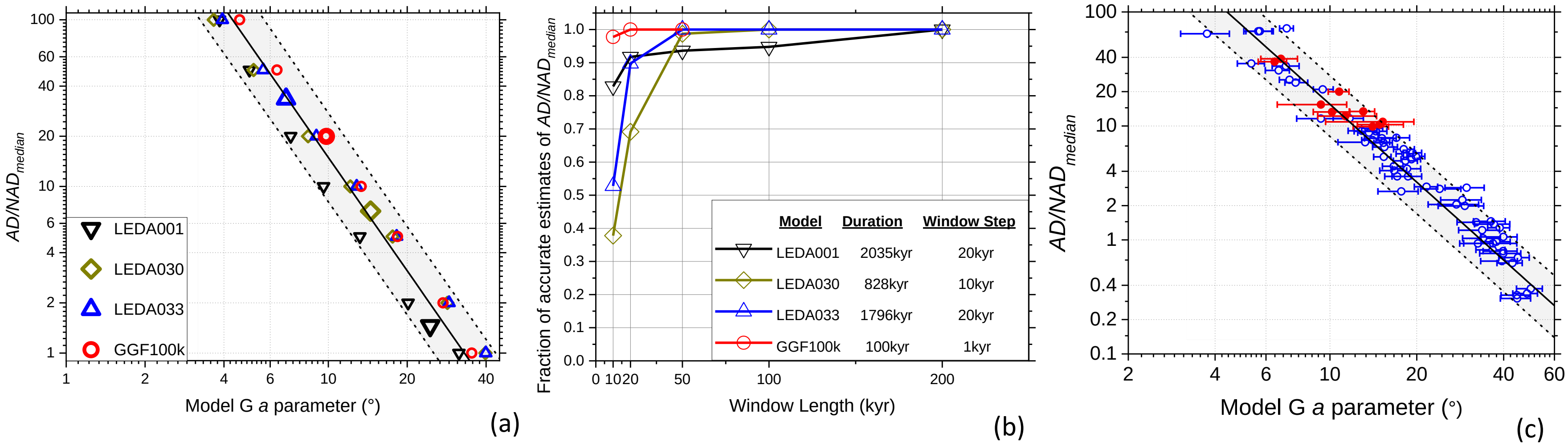

Figure 3: Tests of robustness and usefulness of power law displayed in Figure 2. (a) Effects of arbitrarily rescaling the axial dipole term at every realisation using four models shown in Figure 1. (See supplementary text for details and Supplementary Figure 3 for individual Model G fits). Original model outputs (large symbols) are diverse; rescaled models (small symbols) can have entirely different values of AD/NAD_{median} to the original but the corresponding Model G fit adjusts simultaneously such that each point remains within the 95% prediction bounds derived from Figure 2. (b) Results of a sliding window analysis using time series from the same four models as in Figure 1 . In each case, the sliding window of length given by the x-axis was moved from the start of the time series through to the end in window steps of 1 -20 kyr (adjusted for the total time series length) drawing 15 random timesteps from each of 19 random locations on the surface of the Earth. Estimates of AD/NAD_{median} made using the power law in Figure 2 were defined as accurate if they were within calculated uncertainties of the actual value of AD/NAD_{median} for that specific time window. See Supplementary Figure 5 for individual plots of the AD/NAD_{median} time series and estimates from windows sliding along it. (c) Effects of down-sampling (15 timesteps at each of 19 locations) on 61 dynamo models and 12 observational models on their adherence to the power law shown in Figure 2. Model G *a* parameters were calculated from the downsampled dataset whereas AD/NAD_{median} values were calculated directly from the models using every timestep. The overlaps of the majority of calculated uncertainties on Model G *a* parameters with the prediction bounds ascertained from Figure 2 indicates that this method of estimating AD/NAD_{median} values from the Model G fit is reliable for palaeomagnetically feasible datasets.

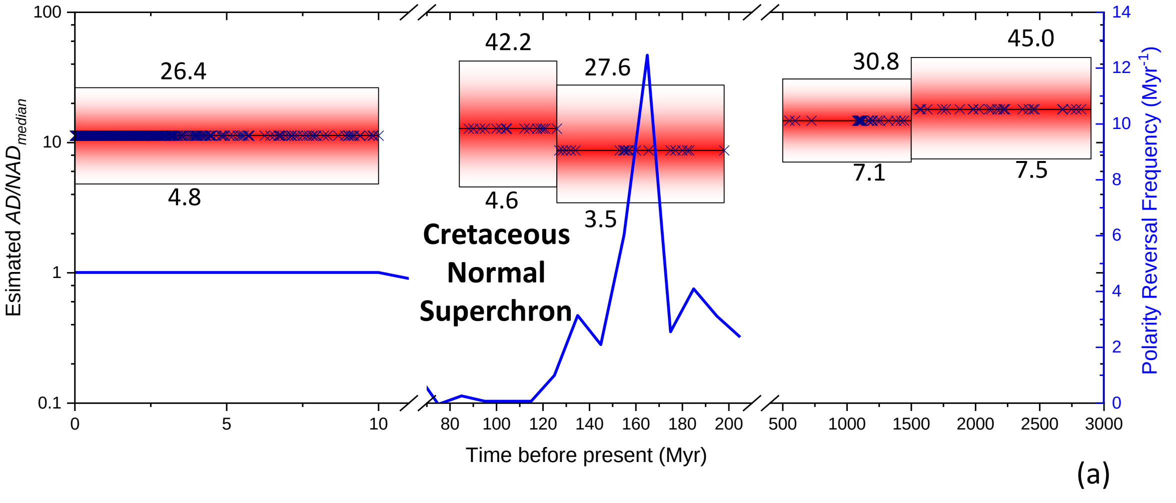

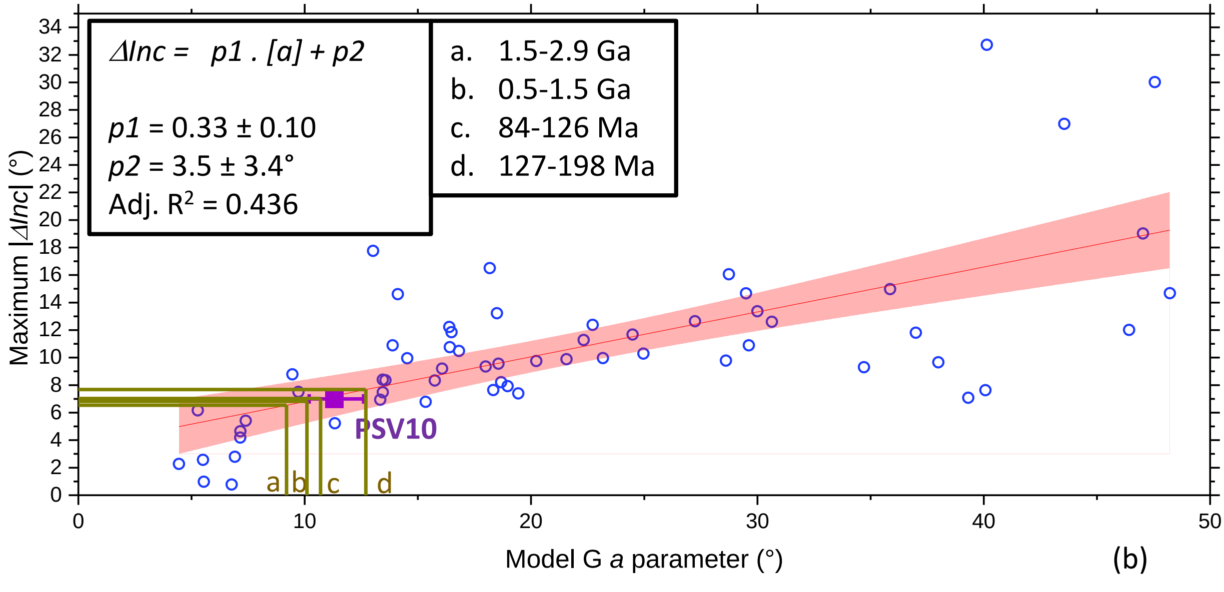

Figure 4: (a) Application of power law in Figure 2 to ascertain first quantitative estimates of axial dipole dominance in deep time (see Table 1). Horizontal range of boxes indicates nominal time range; vertical range indicates uncertainties with numerical bounds provided. Crosses relate to age of one or more rock unit comprising the estimate within the box. Reversal frequency was calculated using 10 Myr bins[38]. (b) Relationship between palaeosecular variation and time-averaged inclination anomaly in outputs of dynamo models (blue circles). Shaded area represents 95% confidence bounds. Dataset from the last 10 Myr[19] (purple square) is shown to fit the linear trend well. Extrapolations of inclination anomalies (*ΔInc*) are made using median *a* parameters for four earlier datasets shown in panel (a).

Time Period	Ref.	$N_{locations}$	Median N_{sites}	Model G *a* parameter (°)	Estimated AD/NAD_{median}
0-10 Ma	19,20	16*	119	11.3 + 1.3/-1.1	11.3 + 15.0/-6.5
84-126 Ma	20	19	24	10.7 + 2.2/-2.4	12.8 +29.4/-8.3
127-198 Ma	20	20	15	12.7 + 1.9/-2.7	8.7 +18.9/-5.3
0.5-1.5 Ga	27	28	17	10.1 ± 0.5	14.7 +16.1/-7.6
1.5-2.9 Ga	27	27	17	9.2 ± 1.1	18.0 +27.0/-10.5

Table 1: Published studies of the Model G a parameter for various time periods allowing estimation of AD/NAD_{median} from the power law shown in Figure 2. $N_{locations}$ refers to the number of locations where S was measured using N_{sites} site-mean palaeomagnetic directions. Uncertainties are reported 95% confidence limits. *In this study, globally distributed VGPs were grouped into 16 latitudinal bins for the purpose of fitting Model G.

Supplementary Text

Theoretical approximation of empirically obtained power law

Here we derive a power law with similar constants to that obtained from our numerical dynamo simulations and observational models using various simplifications and approximations. Specifically, we consider only the case where the non-axial-dipole field comprises the two equatorial dipole terms and therefore neglect all terms with degree > 1. We also assume that Δ_I, the angular distance of the *i*th VGP from the geographic pole, which we denote in units of radians, to only ever be small.

At any one time instance, *i*:

$$\left(\frac{AD}{NAD}\right)_i = \left(\frac{{g_1^0}^2}{{g_1^1}^2 + {h_1^1}^2}\right)_i = cot^2\Delta_i \approx \frac{1}{{\Delta_i}^2} \qquad \text{S1}$$

Since VGP dispersion, *S* is latitude-independent in this scenario, it is equivalent to the Model G parameter a_r, defining S_r at the equator (here subscript *r* denotes the units of radians) :

$${S_r}^2 = {a_r}^2 = \frac{1}{N}\sum {\Delta_i}^2 \qquad \text{S2}$$

An estimate of the degree of axial dipole dominance, AD/NAD_{char}, can then be obtained combining S1 and S2:

$$\left(\frac{AD}{NAD}\right)_{char} \approx \frac{1}{{a_r}^2} \qquad \text{S3}$$

Taking logs:

$$log\left(\frac{AD}{NAD}\right)_{char} \approx -2\log a_r = 2\log\left(\frac{180}{\pi}\right) - 2\log a \qquad \text{S4}$$

Where *a* is the Model G parameter *a* defined in units of degrees

We now have AD/NAD and a_d in a power law form similar to equation (5) in the main text:

$$log\left(\frac{AD}{NAD}\right)_{char} \approx {k_1}^* \log a + {k_2}^* \qquad \text{S5}$$

Furthermore, the derived values of k_1^* (-2) and k_2^* (3.52) are reasonably similar to their empirically-obtained counterparts k_1 (-2.26) and k_2 (3.44). This degree of correspondence is somewhat reassuring as to the robustness of this power law given that AD/NAD_{char} is not the same as AD/NAD_{median} (although the two are expected to be similar in value) and that we have neglected the entire nondipole field in this derivation.

Process for generating rescaled models

In Figure 3a and Supplementary Fig 4, the g_1^0 gauss coefficient (axial dipole) from three dynamo models and the field model GGF100k were rescaled in order to provide a further test of the robustness of the relationship between Model G a values and corresponding AD/NAD_{median} values.

The process for generating each point on Figure 3a (and curve on Supplementary Fig 4) was as follows:

1. For each of the four models, calculate *AD/NAD*$_{median}$ prior to any rescaling and then iterate steps 2 and 3 below using rescaled values (denoted *AD/NAD*$_{median}$*) from the set {1, 2, 5, 10, 20, 50, 100}

2. To obtain each value of *AD/NAD*$_{median}$*, multiply g10 coefficients at all timesteps by a correction factor, *c* using:

   $$c = \sqrt{(AD/NAD_{median}\ /\ AD/NAD_{median}{}^{*})} \qquad \text{S6}$$

   This provides a new time series of g10 coefficients (g10*)

3. Replace g10 terms in the original model's output with g10* keeping all other term identical such that the time series has the new ratio *AD/NAD*$_{median}$*. Apply the process outlined in *Methods* to obtain the best-fitting Model G *a* parameter using this new set.

In every case, modifying *AD/NAD*$_{median}$ by an arbitrary amount simultaneously caused the Model G *a* parameter to shift in a manner consistent with the power law shown on Figure 2.

ID	Model	Ref	Duration (kyr)	Timestep (yr)	AD/NAD_{median}	O/E_{median}	AD/NAD_{TAF}	O/E_{TAF}	*a* (°)	*b*	RMSE (°)
1	BB18	16	-	-	10.3	1.5	72462.6	1.8	11.9	0.22	0.99
2	BB18.z3	16	-	-	9.9	1.5	571.6	0.3	11.6	0.24	1.19
3	BCE19	17	-	-	13.3	3.4	218207.5	0.3	10.3	0.20	1.76
4	TK03.GAD	15	-	-	12.2	2.8	53551.9	6.4	11.1	0.20	1.30
5	CJ98	13	-	-	15.4	2.3	268.2	0.0	8.5	0.21	0.95
6	CP88	14	-	-	13.4	0.4	188.5	0.0	13.4	0.06	1.08
7	GGF100k.1	11	99.8	200	20.0	0.4	96.0	0.4	9.8	0.06	1.34
8	LSMOD.1	7	20.1	50	10.9	0.3	74.7	0.0	13.1	0.13	2.68
9	CALS10k.2	8	10	40	38.8	0.5	199.4	0.1	6.3	0.10	1.48
10	pfm9k.1b	10	8.9	50	36.6	0.6	225.5	0.4	6.4	0.11	1.83
11	gufm	9	0.4	2.5	16.4	0.4	21.2	0.4	6.0	0.00	2.97
12	IGRF	63	0.12	5	10.5	0.5	11.1	0.5	2.3	0.00	1.43

Supplementary Table 1: Summary properties of 12 published observation-based field models. In the case of giant Gaussian Process models (1-6), 10,000 realisations were used. AD/NAD_{median} is defined in the main text. AD/NAD_{TAF} is calculated using the same formula but using a single set of Gauss coefficients which are the arithmetic mean of those at each timestep. *O/E* is defined in ref-5 as the ratio of the sum of Lowes power (*W*)[4] in equatorially antisymmetric (odd) terms (after excluding g_1^0) to W in equatorially symmetric (even) terms. O/E_{median} is the median for all timesteps, O/E_{TAF} makes use of the time-averaged field as for AD/NAD_{TAF}. All are measured at Earth's surface. Parameters *a*, *b* and *RMSE* (root mean square error) refer to fits of Model G[14] to palaeosecular variation data extracted as set out in *Methods*. The lowest rows are shaded grey because the duration of these models are so short that the Model G parameters are almost certainly suppressed; they are therefore not included in any analyses.

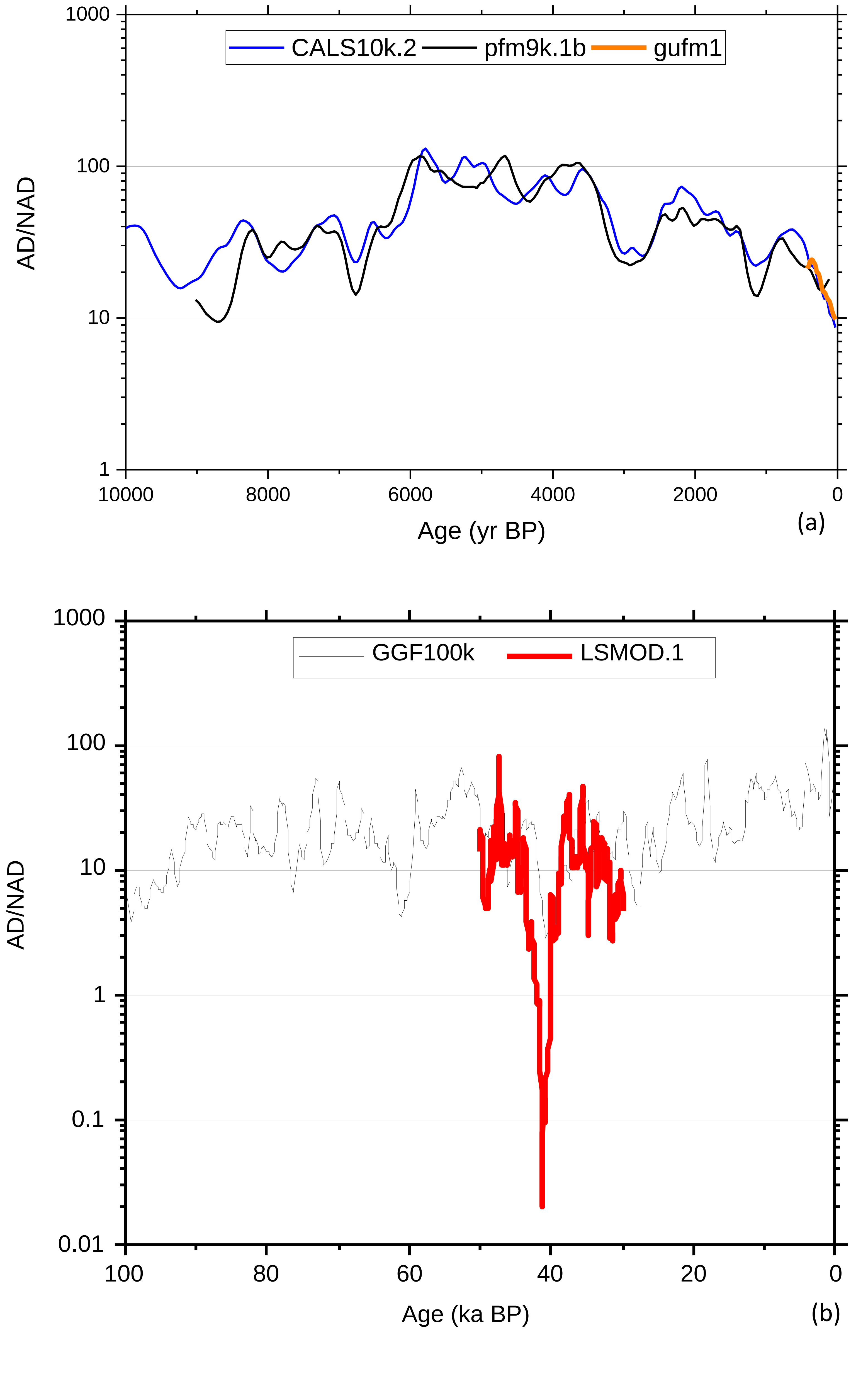

Supplementary Figure 1: Time series of AD/NAD at Earth's surface (note semi-log axes) for (a) gufm1[9]; pfm9k.1b[10]; CALS10k.2[7] and (b) LSMOD[8]; GGF100k[11].

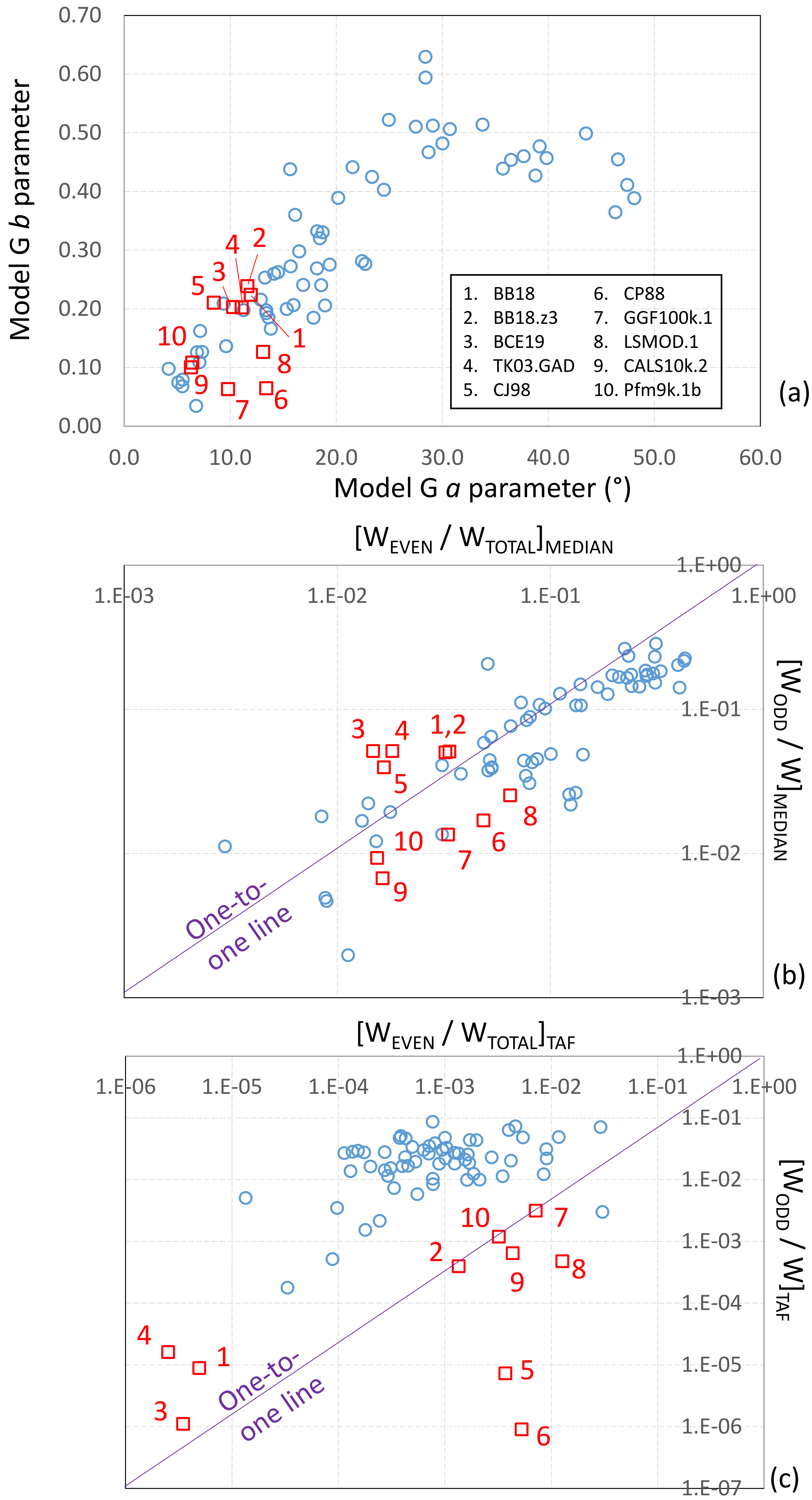

Supplementary Figure 2: Relationships between parameters describing surface field behaviour output from dynamo models (blue) and observational models (red squares). (a). Parameters of Model G –style fits to VGP dispersion results. (b,c) Relative Lowes power associated with Gauss coefficients whose degree and order sum to even and odd values (i.e. equatorially symmetric and antisymmetric terms respectively). In the odd case, the axial dipole is excluded. In (b) the Gauss coefficients are summed at each timestep and the median of the timestep values is used. In (c) a time-averaged field is first constructed by normalising polarity (all terms are flipped when axial dipole is reversed) and taking the mean of each Gauss coefficient; odd and even power sums are then calculated. There is clearly positive covariance in all three datasets. In (a), this indicates the tendency to be that, as equatorial VGP dispersion increases, so does the latitudinal dependence of the dispersion. In (b) scatter around the one-to-one line (purple) indicates that the non-axial dipole field at each time instance tends to be roughly shared between odd and even terms. In (c), the non-axial dipole part of the time-averaged field is shown to be between 1 and 2 orders of magnitude smaller than that, on average, at individual time instances but not equally partitioned into odd and even terms. Specifically, dynamo models tend to favour persistent odd terms whilst observational models tend to favour persistent even terms.

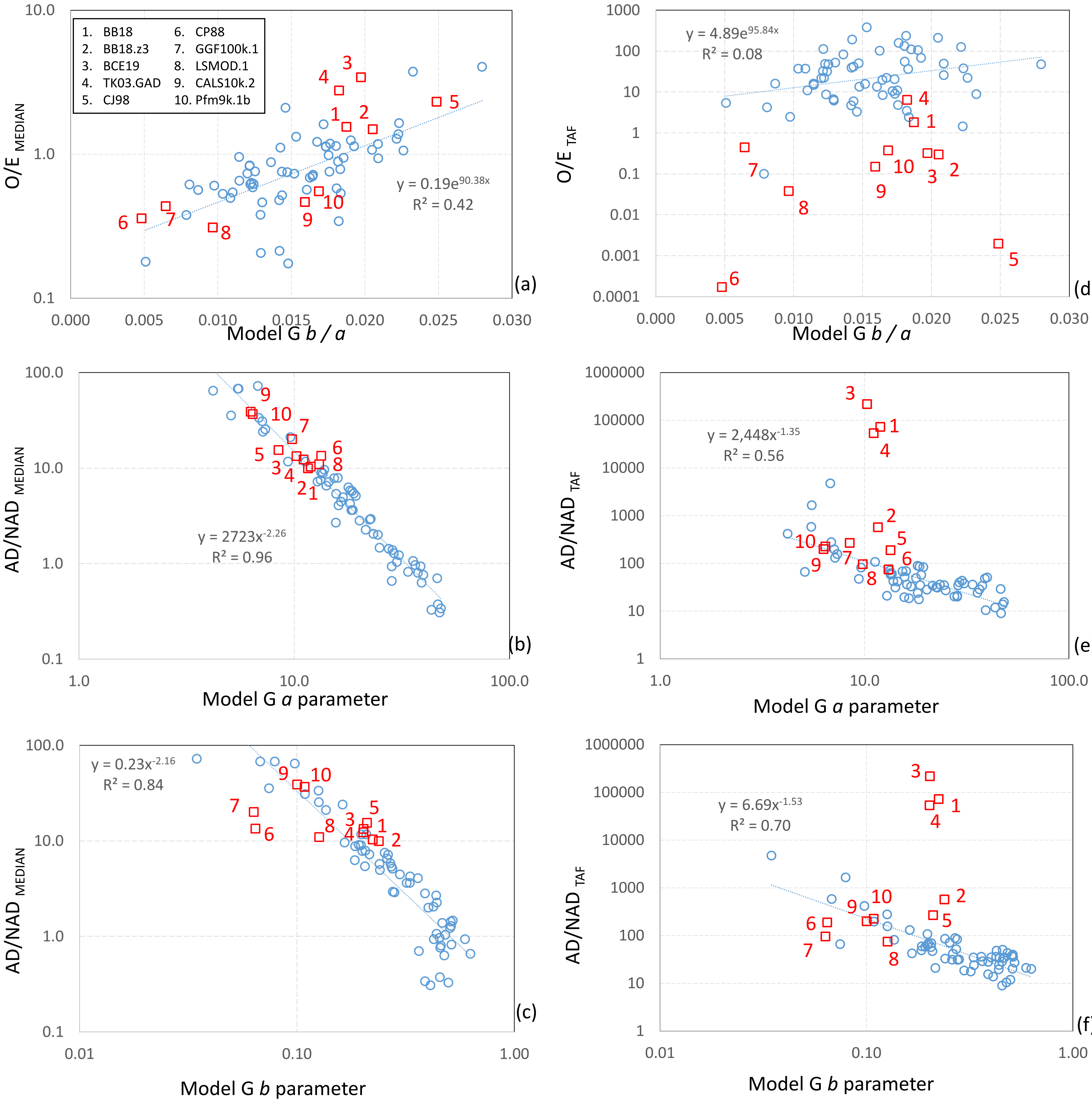

Supplementary Figure 3: Palaeosecular variation descriptors as predictors of surface field morphology described in terms of ratios of groups of Gauss coefficients for dynamo simulations (blue circles) and observational field models (red squares). In all cases, best-fitting lines and equations refer to the dynamo models only. (a, d) Ratio of Model G parameters shown versus ratio of Lowes power associated with groups of odd (excluding g_1^0) and even terms (i.e. equatorially antisymmetric and symmetricterms respectively). (b, e) Model G *a* parameter shown versus ratio of Lowes power associated with g_1^0 and all other terms. (c,f) Model G *b* parameter shown versus ratio of Lowes power associated with g_1^0 and all other terms. (a,b,c) are based on the median Lowes power ratio calculated at every timestep. (d,e,f) are based on the Lowes power ratio of the calculated time-average field (TAF).

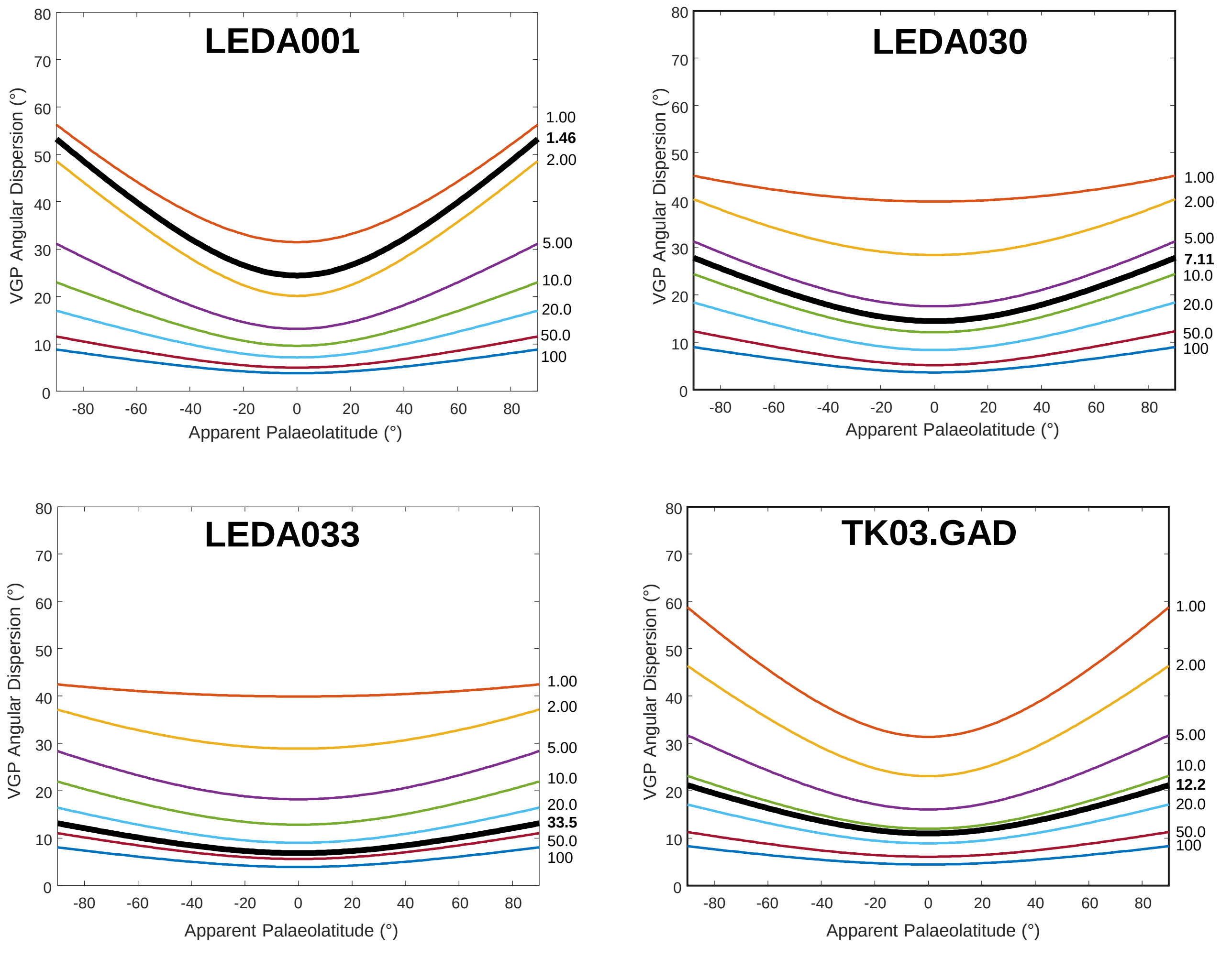

Supplementary Figure 4: Individual Virtual Geomagnetic Pole (VGP) dispersion vs Palaeolatitude plots for Model G datasets summarised in Figure 3a. Original fits are shown in bold and their axial dipole term is rescaled at each realisation to produce the AD/NAD_{median} values shown to the right of each plot. VGP dispersion values at the equator (defined by Model G a parameter in Figure 3a) are similar for all identical AD/NAD_{median} values regardless of the initial dominance of the axial dipole term.

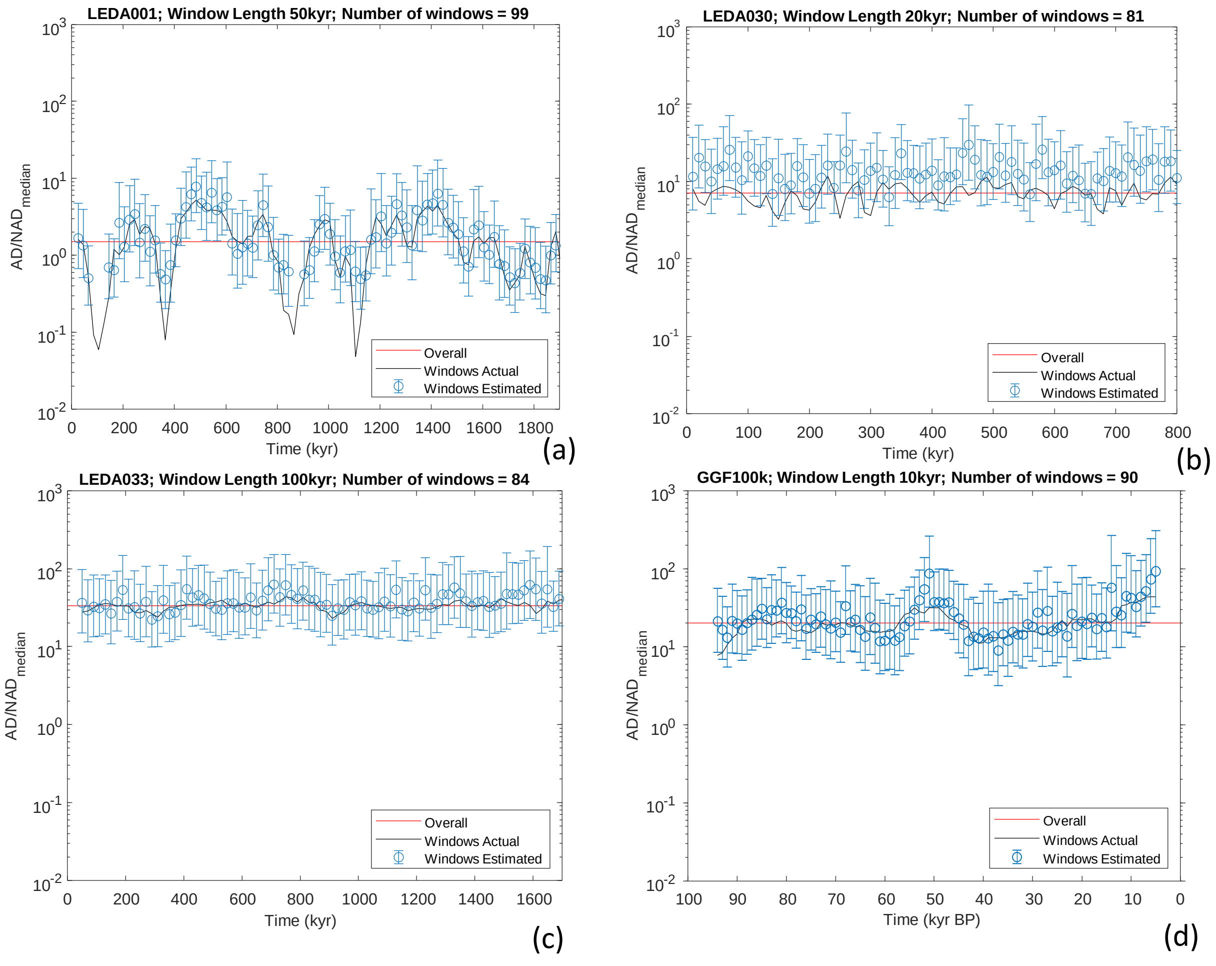

Supplementary Figure 5: Examples of four different time window lengths applied in a sliding window analysis to four different models. Smoothed values of actual AD/NAD_{median} are shown by a black line; individual estimates with uncertainties within windows are shown in blue; red lines show overall AD/NAD_{median} values for each entire model.

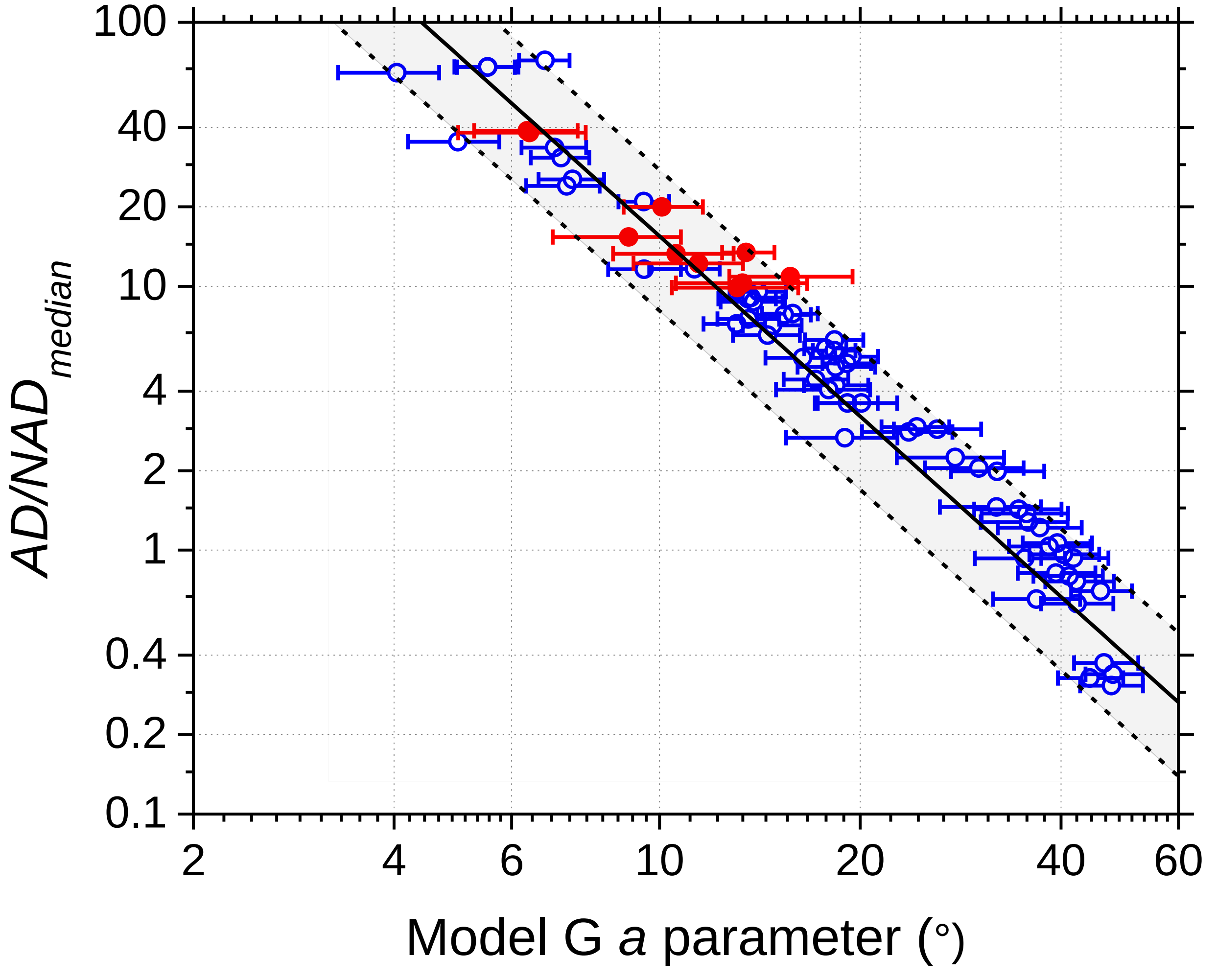

Supplementary Figure 6: An alternative test of downsampling to that presented in Figure 3c. Here, each model was down-sampled (again, 15 random timesteps at each of 19 random locations) 1000 times. The error bars represent 95% of the range of *Model G a parameter* values obtained from the 1000 iterations and circles are median values. Dashed lines are prediction bounds taken from Figure 2.